frontiers in Earth Science

ORIGINAL RESEARCH
published: 11 June 2021
doi: 10.3389/feart.2021.651967

δ^{60}Ni and δ^{13}C Composition of Serpentinites and Carbonates of the Tekirova Ophiolite, Turkey, and Meatiq Ophiolite, Egypt

Anna Neubeck[1], Arjen Boosman[2], Hakan Hosgörmez[3], Dogacan Özcan[3], Arman Boskabadi[4], Magnus Ivarsson[5] and Olivier Rouxel[6]*

[1]Department of Earth Sciences, Uppsala University, Uppsala, Sweden, [2]Department of Earth Sciences, Utrecht University, Utrecht, Netherlands, [3]Department of Geological Engineering, Istanbul University - Cerrahpasa, Istanbul, Turkey, [4]Department of Geological Sciences, Stockholm University, Richardson, Sweden, [5]Swedish Museum of Natural History, Stockholm, Sweden, [6]Ifremer, Plouzané, France

Nickel isotope fractionation patterns in continental ultramafic environments generally show a depletion of δ^{60}Ni in weathered rocks and an enrichment in bedrock samples. The present study focuses on stable Ni isotope fractionation patterns in carbonate-rich, ultramafic ophiolite samples with concomitant fluids at an active serpentinization site in southwestern Turkey, with a comparison to results from an inactive serpentinization site in the Eastern Desert of Egypt with carbonate-rich samples. All solid phase data from the inactive serpentinization area are consistent with previously reported values from serpentinites, whereas the solid precipitates in the active area (SW Turkey) give values slightly heavier than previously reported data. However, the Ni isotopic signatures in the active serpentinization system likely reflect the scavenging of light Ni by iron oxide and carbonate precipitation, as has been previously demonstrated in laboratory coprecipitation experiments. It is also possible that the active system results resemble previous laboratory experimental results that show a relatively strong initial fractionation between fluids and solids, which then diminishes with time due to aging of the precipitates.

Keywords: nickel isotopes, ophiolite, carbonate, serpentinization, methane seep, carbon isotopes, iron oxide

OPEN ACCESS

Edited by:
Fang-Zhen Teng, University of Washington, United States

Reviewed by:
Xiangli Wang, University of South Alabama, United States
Desiree Roerdink, University of Bergen, Norway

****Correspondence:***
Anna Neubeck
anna.neubeck@geo.uu.se

Specialty section:
This article was submitted to Geochemistry, a section of the journal Frontiers in Earth Science

Received: *11 January 2021*
Accepted: *31 May 2021*
Published: *11 June 2021*

Citation:
Neubeck A, Boosman A, Hosgörmez H, Özcan D, Boskabadi A, Ivarsson M and Rouxel O (2021) δ^{60}Ni and δ^{13}C Composition of Serpentinites and Carbonates of the Tekirova Ophiolite, Turkey, and Meatiq Ophiolite, Egypt. Front. Earth Sci. 9:651967. doi: 10.3389/feart.2021.651967

INTRODUCTION

Several studies have investigated stable Ni isotope compositions in ultramafic/mafic rocks to better understand the geochemical cycling of Ni in natural environments (Cameron et al., 2009; Gueguen et al., 2013; Ratié et al., 2015; Spivak-Birndorf et al., 2018). It has been shown that the world's major rivers are enriched in heavier Ni isotopes (+0.29 to +1.34‰) compared with solid Ni sources (+0.15‰), which, in contrast, are depleted in ^{60}Ni (Cameron and Vance, 2014). The Ni isotopic composition of unweathered mafic and ultramafic rocks (such as gabbro, basalt, peridotite, dunite, and serpentinized varieties) falls within a relatively narrow range of −0.13–+0.32‰ (Gall et al., 2013; Gueguen et al., 2013; Ratié et al., 2015; Spivak-Birndorf et al., 2018). Weathering of mafic and ultramafic rocks results in extensive formation of clays and iron oxides, which have both been shown to preferentially adsorb light Ni (Wasylenki et al., 2015; Spivak-Birndorf et al., 2018). In contrast, Ni-rich hydrous Mg-silicates, such as garnierite, a common product of serpentinization, show enrichment in heavy Ni isotopes (Spivak-Birndorf et al., 2018). No directed analyses were

performed on other common natural serpentinization products such as brucite (Mg-hydroxide) or Mg–Ca carbonates. However, experimental adsorption and coprecipitation of calcite and Ni have shown a preferential adsorption/incorporation of light Ni into calcite (Alvarez, 2019) with a $\Delta^{60}Ni_{fluid-solid}$ as low as −1‰. Strong hydration of the divalent Ni ion at high calcite precipitation rates is one explanation for this behavior. It is still unknown how aging of calcite influences the isotope signature of Ni isotopes in experimentally precipitated calcites. In a coprecipitation study on Mn-oxides and Ni by Wasylenki et al. (2019), it was shown that the initial, strongly fractionated $\Delta^{60}Ni_{fluid-solid}$ signature diminished after a few weeks due to aging. This effect would potentially obstruct the possibility of finding natural counterparts unless samples were analyzed immediately after collection. Aging is a physical transformation process in which the precipitated minerals may change mineralogy, morphology and composition with time. Element substitution and ratios may change significantly with time, as shown by Wasylenki et al. (2019), where the concentration and thus the isotopic signature of Ni in the mineral precipitate changes.

Terrestrial areas of active serpentinization are commonly associated with low vegetation, high-pH fluids, high dissolved Ca and Mg concentrations, reduced gas seepage, and extensive secondary mineral precipitation (Etiope et al., 2011). This study focuses on the Tekirova ophiolite (near Antalya, Turkey), where localized and diffusive fluxes of abiotically formed CH_4 gas seep from the rock as a product of active low-temperature serpentinization (Etiope et al., 2011; Etiope and Sherwood Lollar, 2013). High pH and extensive carbonate precipitation are common features of the area. As a comparison, a serpentinized carbonate-rich ophiolite with no active serpentinization in the Meatiq area, Eastern Desert (ED), Egypt, is investigated. In order to better understand the geochemical cycling of Ni in carbonate-rich ultramafic and mafic rocks, this study aims to investigate the C and Ni isotopic differences between active and inactive serpentinization systems with extensive precipitation to evaluate the influence of secondary mineral precipitation on the fractionation of stable Ni isotopes. Carbon isotopes were additionally measured to evaluate the possible influence of microorganisms on the Ni isotopic fractionation. The two field sites of the current study contain fresh and aged carbonate precipitates as well as serpentinites, brucites, and iron oxides and may therefore display a wide variety of $\delta^{60}Ni$ signatures, from very depleted, associated with iron oxides, to enriched, commonly associated with the meteoric waters flowing on the ophiolite surface (Cameron and Vance, 2014). Both study sites have been or are currently subjected to carbonation, a process in which igneous rocks interact with fluids rich in CO_2, resulting in carbonate precipitation.

MATERIALS AND METHODS

Geological Setting of the Tekirova Ophiolite Outcrop

The studied site is a terrestrial methane gas seep at the Tekirova ophiolite in Turkey. The Tekirova ophiolite is a part of several N–S trending zones of rocks associated with rifting, basin formation, and development of passive margins (Hosgörmez, 2007). Tekirova is located in the tectonic contact zone between the western Kemer Zone serpentines and the Tekirova Zone carbonates, all forming part of the larger Antalya Complex, which was emplaced onto the continental plate in the Late Cretaceous. During the emplacement, ophiolitic material was incorporated into the continental carbonates, initiating a strong serpentinization process and secondary carbonate precipitation. Well-preserved ultramafic to mafic cumulate rocks crop out at Çıralı, where serpentinization-induced gas seeps are located (Hosgörmez, 2007). The western Kemer Zone consists of a Mesozoic carbonate platform that overlies Ordovician–Triassic sedimentary rocks. The eastern Tekirova Zone, on the Mediterranean coast, is composed of Cretaceous ophiolite with well-preserved olivine-rich ultramafic to mafic cumulates as well as peridotite, gabbro, serpentinized harzburgite with minor lherzolite, podiform dunite, and chromitite (Aldanmaz et al., 2009). Between the two zones lies the Tekirova fault, where serpentines and metasediments are the dominant rocks. Below the fault are several rock formations that can generate hydrocarbons: the Sapandere bituminous shale (Ordovician–Silurian), the Beydağları limestone (Lower Mesozoic), and the Pamucakyayla siltstones and coal (Carboniferous). An extensional phase started in the late Pliocene and is ongoing, which may form pathways for gas seepage due to the resulting increase in the permeability of the rocks (Demirel and Gunay, 2000). Active serpentinization is associated with the ophiolitic outcrop, forming extensive seeps of methane gas continuously flowing from the rocks, visible as continuously burning flames. Active serpentinization is also evident in the mineralogy of the area, which shows serpentine clasts in host minerals, indicative of serpentinization reactions at greater depths involving temperatures between 200 and 300°C (Hosgörmez et al., 2008; Etiope et al., 2011; Etiope and Sherwood Lollar, 2013). Serpentine, brucite, and magnetite were produced during hydration reactions of olivine and pyroxene. The mineral textures also show that further serpentinization reactions within the ophiolite proceed at low temperatures (below 200°C) and are currently active, forming the secondary carbonate veins (Zwicker et al., 2018). Earlier studies have reported that the fluids in the area have pH values of 7–12 and gas compositions of 87% CH_4, 7.5–11% H_2, 2–4.9% N_2, 0.57% light alkanes, 0.01–0.07% CO_2, and 80 ppm He (Woodcock and Robertson, 1977; Meyer-Dombard et al., 2015. The sources of these gases are both abiotic and biotic, as shown by stable isotopic analyses (Hosgörmez et al., 2008). The most common minerals in the rocks at Tekirova are, in decreasing order of bulk abundance, serpentine (lizardite–chrysotile), brucite, calcite, aragonite, magnesian calcite, chromite, rutile, and ferromanganese (Hosgörmez, 2007).

Geological Setting of the Meatiq Ophiolite Outcrop, Egypt

The Meatiq area is located about 40 km west of the Red Sea within the ED of Egypt. Ophiolitic rocks of the Meatiq area comprise mainly serpentinite, including lizardite- (Lz-) and antigorite-

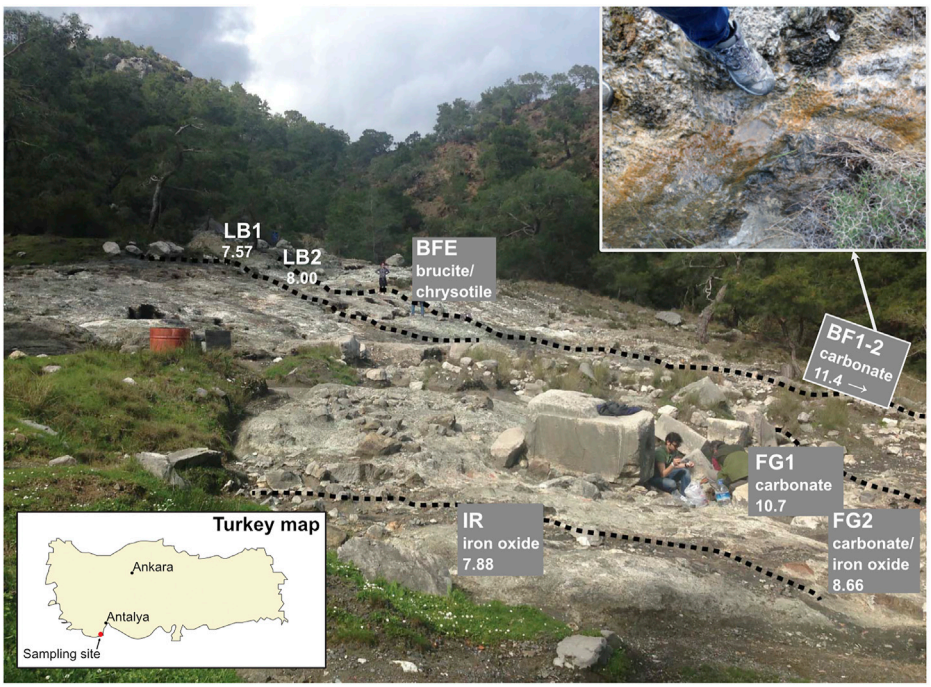

FIGURE 1 | Chimaera outcrop location in the Antalya region. Map of Turkey in the lower left panel and a zoomed-in overview over the outcrop and the sample locations in the upper right panel. The bright white area and the surrounding grayish area are the exposed ophiolite with no vegetation. Dotted lines represent small, meandering streams located on the ophiolite outcrop.

TABLE 1 | Overview of samples collected at Tekirova and Meatiq.

Sample site	Sample name	Number of water samples	Number of rock samples	Sample description
Tekirova	JSB	1	0	Large river flowing north of Yanar Creek
Tekirova	SB	1	0	Small river flowing through the carbonates and close to the southern part of Chimaera
Tekirova	LB1 and LB2	2	2	Small stream that meanders over the ophiolite from a source uphill
Tekirova	FG1 and FG2	2	2	Small stream that meanders over the ophiolite and has a source uphill and another source at the exposed sampling site
Tekirova	IR	1	1	Small stream that meanders over the ophiolite and has a source uphill, with sediment with a strong rusty color
Tekirova	BFE	0	1	Dry rocks close to the LB1 and LB2 sites
Tekirova	BF1, BF2	2	2	—
Meatiq	Me5	0	1	ATG serpentinite
Meatiq	Me6	0	1	ATG serpentinite
Meatiq	Me7	0	1	ATG serpentinite
Meatiq	Me8	0	1	ATG serpentinite
Meatiq	Me9	0	1	ATG serpentinite
Meatiq	Me21	0	1	LZ serpentinite
Meatiq	Me22	0	1	LZ serpentinite
Meatiq	Me23	0	1	LZ serpentinite
Meatiq	Me24	0	1	LZ serpentinite
Meatiq	Me01	0	1	Talc-rich
Meatiq	Me14	0	1	Talc-rich
Meatiq	Me17	0	1	Talc-rich

(Atg-) rich serpentinites, as well as metagabbro and metabasalt and their metamorphosed and carbonate-altered products such as talc-rich rocks, talc-carbonate rocks, and listvenites. The degree of carbonate alteration is more intensive in Atg-serpentinites than in Lz-serpentinites. The ophiolitic rocks from the Meatiq area are included in this study as a reference

representing ophiolitic rocks with no active serpentinization. The ophiolite emplacement occurred after approximately 736 Ma. Alteration of the ophiolite, such as serpentinization and carbonation due to interaction with migrating carbonate-rich fluids (Stern and Gwinn, 1990), occurred at ~600 Ma (Boskabadi et al., 2017).

Sampling

A total of eight solid samples and nine water samples were collected at Tekirova in Turkey, and 12 solid samples were collected at Meatiq in Egypt (**Figure 1**; **Table 1**). Sediment samples were collected using a sterile spatula and stored in sterile Falcon tubes.

Tekirova

The sampling sites are situated at an exposed area located on the Tekirova ophiolite outcrop, north of Çıralı, Antalya, Turkey. Flames of burning gas are scattered around the site, and three small fluid seeps meander downslope over the outcrop. The site is mostly dry during the year, but during the rainy season (November–February), small streams and ponds of standing water are present not only on the primary sampling site but also close to other sampling sites located at higher elevations. On-site pH measurements were obtained using a hand-held pH meter (pHTestr 30, Thermo Scientific, Eutech Instruments Pte. Ltd., Germany, with an uncertainty of approximately 0.2 pH units). The Tekirova samples were collected in February, during the rainy season, which was necessary in order to be able to collect any fluids since the site is often completely dry. Fluid samples for trace element analyses were collected from sites JSB, SB, LB1, LB2, FG1, and FG2 (**Table 1**) by withdrawing fluids using sterile syringes and were injected into acid-washed (3 M HCl for 24 h) 10 ml plastic tubes and sealed. After collection, all samples (except samples for Ni isotopes, which instead were centrifuged) were filtered through a pre-cleaned cellulose nitrate 0.2 μm filter into a pre-cleaned plastic tube and stored at +8°C. Sediment samples (FG1, FG2, and IR) were collected at the same time as the water samples by scooping the material into sterile plastic tubes using pre-cleaned plastic spoons. Solid samples for mineral analyses were collected using a rock hammer and plastic bags and were collected at the same sites as the fluid samples.

Meatiq

The Meatiq area is located about 40 km west of the Red Sea, Egypt. Ophiolitic rocks of the Meatiq area comprise mainly serpentinites and their altered products such as talc-rich rocks, talc-carbonates, and listvenites. U–Pb dating of zircons from an ophiolitic gabbro (Fawakhir, located SW of the Meatiq area) suggests a crystallization age of 736.5 ± 1.2 Ma for the ophiolites in this region (Andresen et al., 2009). A detailed description of the geology of the area can be found in Boskabadi et al. (2017).

The samples from the Meatiq area were collected at three main localities from quarry and/or roadside outcrops and were selected based on the type of serpentinization, the extent of carbonation, and the carbonated products. A detailed description of the sampling in the Meatiq area can be found in Boskabadi et al. (2017).

Analysis and Procedures

Analysis of Elements in Solution

The dissolved elemental compositions of the fluid samples were measured using inductively coupled plasma-optical emission spectroscopy (ICP-OES, Spectro, Varian Vista AX), with Ar as the carrier gas, at the Department of Geological Sciences, Stockholm University, Sweden. Approximately 10 ml of filtered fluid sample were mixed with 0.5 μl > 65% HNO_3 (Sigma-Aldrich, puriss.) prior to analysis. The analytical error was ~4%. All measurements were obtained using multi-element matrix-matched standards and certified standards (NIST 1640a) as a control for the multi-element standards (LGC-Promochem) used for inductively coupled plasma mass spectroscopy (ICP-MS).

Optical Microscopy

Optical microscopy of thin sections was conducted using a Leitz polarization microscope to determine mineralogy. An Olympus BX-51 fluorescence microscope equipped with an Olympus DP-71 digital camera was used to determine the biologic influence and/or presence in the samples (excitation wavelength of 395–440 nm, emission >470 nm), where a green color represents carbonate precipitates (dark green) and a yellow color (dark yellow) represents organic matter (Dupraz et al., 2013).

Raman Spectroscopy

Raman spectra were collected using a confocal laser Raman microspectrometer Horiba instrument (LabRAM HR 800; Horiba Jobin Yvon) equipped with a multichannel air-cooled (−70°C) 1,024 × 256 pixel charge-coupled device (CCD) detector. Acquisitions were obtained with an 1,800 lines/mm grating. Excitation was provided by an Ar-ion laser source (λ = 514 nm). Spectra were recorded using a laser power of 0.1–1 mW at the sample surface. A small quantity of the sample material was placed on a glass slide on an Olympus BX41 microscope coupled to the instrument. The laser beam was focused through a 100× objective to obtain a spot size of about 1 μm. Collection times for the Raman spectra were 10 accumulations of 10 s each. The accuracy of the instrument was controlled by repeated use of a silicon (Si) reference with a Raman line at 520.7 cm^{-1}. The Raman spectra were obtained with LabSpec five software.

Scanning Electron Microscopy

Surface composition and topography were analyzed semi-quantitatively on an XL30 environmental scanning electron microscope (ESEM) with a field emission gun (FEG). The ESEM was equipped with an Oxford X-Act energy dispersive spectrometer (EDS), a backscatter electron detector (BSE), and a secondary electron detector (SE). Peak and elemental analyses were performed using INCA Suite 4.11 software. None of the samples were coated.

Carbon Analysis (Dissolved Inorganic Carbon, Dissolved Organic Carbon, and Stable Isotopes)

Stable carbon analyses were performed to investigate the influence of microorganisms on the secondary mineralization

and the fluids. Isotope analysis of dissolved inorganic carbon (DIC) were made by direct injection of 5 ml of water sample into 12 ml septum-seal glass vials (Labco Limited, cat. No. 238 W) containing 100 µl of 85% H_3PO_4, and flushing with He gas (100 ml/min) for 5 min. The method used for dissolved organic carbon (DOC) is described in detail in Lang et al. (2012). A volume of 4 ml of a sample or standard was transferred into an exetainer vial using a disposable borosilicate pipette, and 1 ml of the oxidizing agent was then added. The samples were acidified to pH < 3 with 8.5% H_3PO_4 (85% Merck Analysis grade orthophosphoric acid; Merck, Darmstadt, Germany) and diluted by a factor of ten with Milli-Q water (Millipore, Billerica, MA, United States). To remove inorganic carbon, high-purity helium was bubbled (60 ml/min) through the sample manually for 10 min by piercing the septum with a flushing needle. The septum was also pierced with a second needle for the output gas stream. This outlet needle was connected to a copper tube whose open end was submerged in water to prevent any backflow of atmospheric CO_2 into the sample. The DIC and DOC analyses were performed at the Department of Environmental Science and Analytical Chemistry (ACES), Stockholm University, using a Gasbench II coupled to a MAT 253 mass spectrometer, both from Thermo Scientific. Measurement reproducibility was calculated to be better than 0.1‰ for $\delta^{13}C$. Solid sample analyses were performed using an Elemental Analyzer NC 2500 (Carlo Erba) coupled via a split interface to a mass spectrometer (DeltaV Advantage, Thermo Scientific). Precision and accuracy were monitored by reference to long-term analyses of laboratory and international standards. Results are reported as δ‰ values relative to the VPDB scale for $\delta^{13}C$.

Carbon isotope analyses of the Meatiq samples were carried out on the carbonate (mainly magnesite) fraction of serpentinite whole-rock samples (see Boskabadi et al., 2017, for more details).

Ni Isotopic Reagents and Material

Nickel isotopic analysis was performed in a clean room (Class 1000, or ISO-6) at the Ifremer Centre de Bretagne, Brest, France, following the method described by Gueguen et al. (2013) and using a double spike method. Samples and standards (NIST SRM 986) containing Ni concentrations of 0.5–1 µg Ni were evaporated on a hotplate. The spike (containing equal proportions of ^{61}Ni and ^{62}Ni) was then added to all samples and standards at a Ni_{sample}/Ni_{spike} ratio of one and re-evaporated to dryness.

Sample Preparation and Rock Digestion

Rock and water samples were digested in a mixture of HCl-HNO_3 in polytetrafluoroethylene vials and evaporated until dry, followed by addition of HF (28 mol L^{-1} trace metal grade or Suprapure grade) to dissolve all solid remnants. The samples were then evaporated to dryness at a temperature of 70–80°C. The HF treatment step was repeated to achieve complete digestion of non-siliceous rocks and ensure removal of potential fluorides formed in the course of the first dissolution step for siliceous materials. Ni concentrations were re-determined before Ni elution using an ICP-Quadrupole (ICP-Q-MS, X-series II) at Pôle Spectrométrie Océan, Brest. Aliquots (<1 ml) were withdrawn from the water samples and rock solutions and diluted with 0.28 M HNO_3 to a final volume of 10 ml, and Ni concentrations were then measured. With known element concentrations, an optimal concentration of the double spike could be added to trace possible interfering elements.

Sample Purification

Dry sample–spike residues were dissolved in 1 ml 0.24 M HCl. Thereafter, 0.3 ml 1 M ammonium citrate and 125 µl concentrated ammonia were added to increase pH. Approximately 0.5 ml wet Ni-spec resin (Ni Eichrome) was loaded into polypropylene columns. The resin was then washed with 6.5 ml Milli-Q water and 4.5 ml of 0.2 M ammonium citrate +0.45 M ammonia and capped. An additional 0.5 ml of the 0.2 M ammonium citrate +0.45 M ammonia solution was added to buffer the resin pH to ~9. The prepared sample solution was then loaded onto columns containing dimethylglyoxime (DMG) molecules, which at pH < 8 form a Ni–DMG complex that is retained in the resin. The resin was resuspended, increasing the active surface area and rate of complexation, and left for 1 h. The Ni yields through the column were close to 100%, implying that the 1 h equilibration time was sufficient. The caps were removed, and the columns were allowed to drain. After draining, 2.2 ml of the 0.2 M ammonium citrate +0.45 M ammonia solution was added twice, at intervals of 15 min, to wash out Fe and other matrix elements. 2.2 ml of Milli-Q water was added three times at intervals of 15 min to wash out excess ammonium citrate and ammonia salts. Ni was then collected in 6.6 ml of 3 M HNO_3 (added in three applications of 2.2 ml at 15 min intervals). The collected Ni fractions were then dried down on a hot plate at ~95°C overnight. The dry sample residue was then dissolved in 1 ml of 0.3 M HNO_3 for isotopic analysis.

Mass Spectrometry

Ni isotopic compositions were determined using a Thermo Scientific™ Neptune multicollector inductively coupled plasma mass spectrometer (MC-ICP-MS) at the Ifremer Centre de Bretagne in Brest, France. Samples and standards were introduced via an ApexQ MicroFlow PFA-50 self-aspirating nebulizer at an injection rate of ~60 µl min^{-1}. The sample and skimmer cones were made of Ni, but ^{58}Ni intensities of the blanks indicated that no Ni was contributed from the cones, as demonstrated previously (Moynier et al., 2007; Fujii et al., 2011; Gueguen et al., 2013; Neubeck et al., 2021).

Each set of samples was run twice. A short preliminary run (10 cycles, each lasting 4 s) was performed to better determine Ni, Fe, and Cu concentrations. For every sample, there was a standard with a similar concentration and $Ni_{spike}/Ni_{natural}$ ratio. Samples were generally grouped in sets of 2–5 samples, preceded and succeeded by one bracketing standard of NIST SRM 986. In the second run, performed to obtain high-precision isotope data, each sample was measured through five blocks of 10 cycles with 4 s of integration time apiece, separated by an instrument rinse of 10 cycles with 4 s of integration time. The instrument can very precisely measure samples with concentrations over 0.03 ppm Ni, with 2SE < 0.1. Lower concentration measurements yield slightly larger uncertainties in δ-values, with 2SE ≈ 0.1‰. Only

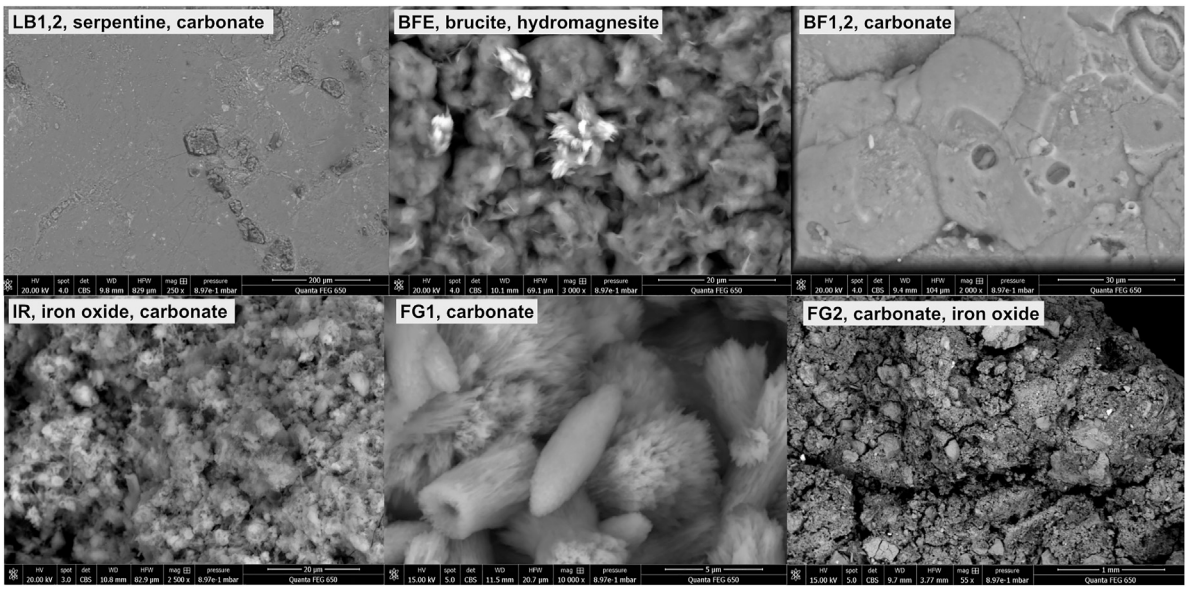

FIGURE 2 | ESEM images of the Tekirova samples, representing common features of the samples. The upper panels show rock samples (LB1-2, BFE, and BF1-2), and the lower panels show sediment samples (IR, FG1, and FG2).

concentrations under 0.01 ppm have extremely high uncertainties exceeding 1‰ (Gueguen et al., 2013). Ni concentrations in rock samples were very high (>10 ppm), and the Ni concentrations in water samples were generally sufficient for precise measurement.

Ni Isotope Data Reduction

Nickel isotope compositions of samples are expressed using the delta (δ) notation, in which the isotopic ratio of the sample is normalized to that of the NIST SRM 986 bracketing standard, following the equation:

$$\delta^{X}\mathrm{Ni}_{\mathrm{sample}}\ (‰) = \left(\frac{{}^{X}\mathrm{Ni}/{}^{58}\mathrm{Ni}_{\mathrm{Sample}}}{{}^{X}\mathrm{Ni}/{}^{58}\mathrm{Ni}_{\mathrm{NIST\ SRM\ 986}}} - 1\right) \times 1000,$$

where X denotes either the ^{60}Ni, ^{61}Ni, or ^{62}Ni isotope (^{64}Ni was not considered in this study). The data presented in this study is described using the ^{60}Ni/^{58}Ni ratio given as δ^{60}Ni. The Ni isotopic compositions of samples were then calculated using the double spike calculation template from Gueguen et al. (2013). The NIST SRM 986 standard was passed through columns four separate times, yielding an average value and external reproducibility for the method of −0.01 ± 0.08‰. Procedural blanks yielded an average amount of Ni of approximately 4 ng.

RESULTS

Tekirova—Mineralogy

Tekirova host rock is composed of strongly serpentinized peridotite with extensive precipitation of iron oxides and carbonates (Hosgörmez et al., 2008; Meyer-Dombard et al., 2015). According to optical microscopy analyses and SEM, the LB samples were dominated by serpentine minerals with minor carbonate precipitates (mainly calcite and minor amounts of aragonite, **Figure 2**; **Supplementary Figure S1**). The BFE sample was dominated by brucite and hydromagnesite with minor amounts of carbonates (**Supplementary Figure S2**), whereas the BF1 and BF2 samples were almost completely dominated by carbonates (**Supplementary Figure S3**). The IR, FG1, and FG2 samples consisted of loose sediments; IR and FG2 consisted of iron oxides and carbonates (**Supplementary Figures S4, S5**), while FG1 consisted purely of carbonates (**Supplementary Figure S6**).

The BF samples are dominated by concentric layers of calcite. Fine and coarse-grained layers of carbonate occur with sharp contacts from yellow to dark yellow/brown, fibrous, and mesh-textured chrysotile. Micro-stromatolites and microspheres (Ø = 20–25 μm) with layers of calcite alternating with organic material are abundant in the samples, and green fluorescence was used to distinguish between the calcitic and organic material (**Figure 3**). Distinct differences between organic and abiotic (chemically precipitated) layers could be observed by Raman spectroscopy and fluorescence microscopy.

Sample IR is completely covered by microorganisms, and organic compounds, cells, and filaments are visible in the SEM images and cover the entire sediment surface (**Figure 4**). The Raman spectra of the IR sample show carbonaceous matter and iron oxides.

Major and Minor Elemental Composition of Tekirova Fluids

The LB samples show a slight downhill increase in pH from 7.6 to 8.0, whereas the FG samples show the opposite trend of a downhill decrease in pH from 10.7 to 8.7. Both BF1 and BF2 show a very high

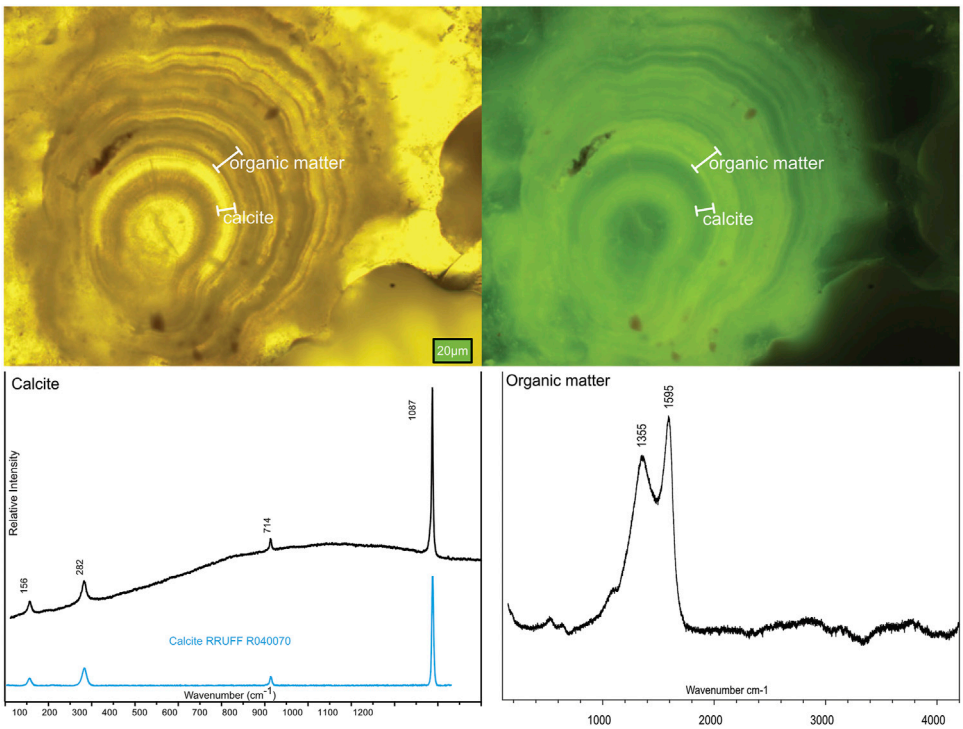

FIGURE 3 | Mineralogy of the samples measured using optical microscopy (fluorescence) and Raman spectroscopy, where the upper panels show the laminations of alternating carbonate and organic carbon in the BF1-2 samples, and the lower panels show the corresponding Raman spectra.

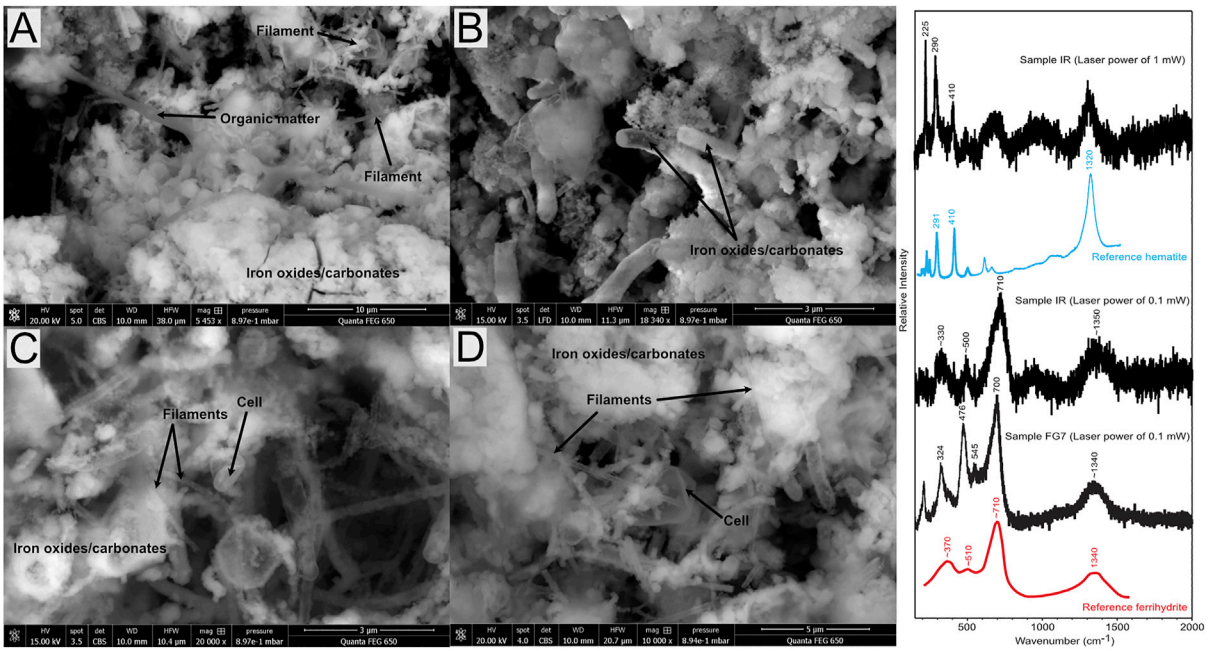

FIGURE 4 | ESEM backscatter images showing colonization of microorganisms covering the IR sample, on which both filament and round cells are visible. **(A)** Distribution of filaments, minerals, and organic matter; **(B)** tube-shaped iron oxide/carbonates in the samples; **(C,D)** more detailed images of the sample, with clearly visible cells and filaments.

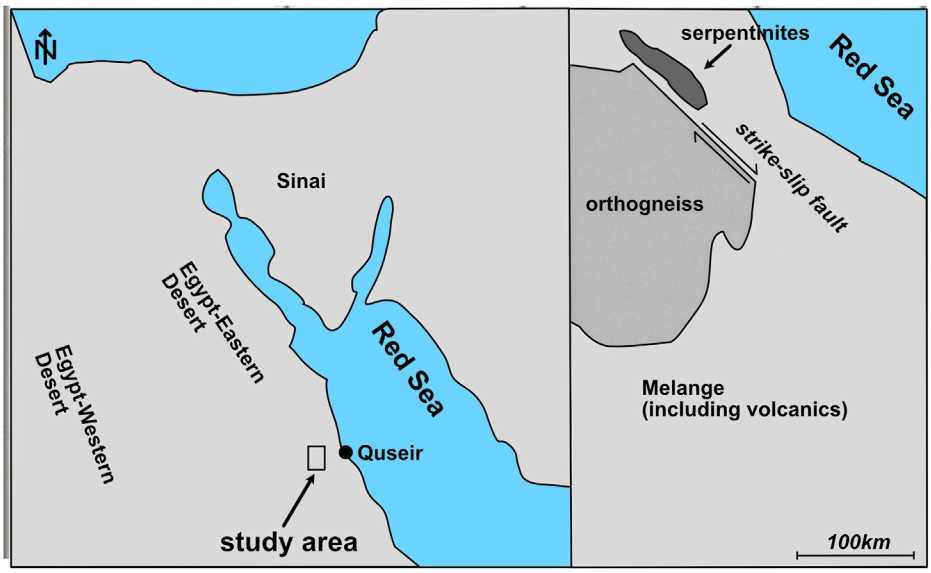

FIGURE 5 | Map of the Meatiq sampling area, which is close to the city of Quseir by the Red Sea. The samples were collected from an outcrop of serpentinites within an area of mélange including volcanics, north of the Um Baánib orthogneiss.

pH of 11.4. The IR sample has a pH of 7.9, and the JSB and SB river samples give pH values slightly above neutral, of 8.0–9.5, respectively. The color changes from white to red in the FG1 and FG2 samples is coupled with a strong increase in Fe from 5.6 to 83.5 ppm and a decrease in Ca from 73.1 to 41.1 ppm. The concentration of Ni in the fluids decreases downhill from 4.5 to 0.8 ppm at LB1 and LB2, respectively, whereas the opposite can be observed in FG1 and FG2, where the Ni concentration increases from 0.3 to 4.5 ppm. The rest of the samples show relatively similar Ni concentrations of around 0.4 ppm, except BF2, which has a slightly higher Ni concentration of 1.1 ppm.

Meatiq Mineralogy

Three types of rock samples were collected in the Meatiq ophiolite in Egypt (**Figure 5**): 1) Lz-serpentinite composed mainly of lizardite and later chrysotile veinlets with minor carbonate, traces of chlorite, and bastite pseudomorphs; 2) Atg-serpentinite consisting mainly of antigorite and carbonate with minor talc and/or clinochlore; and 3) talc-rich rock, composed mainly of talc with minor amphibole, clinochlore, and/or quartz-carbonate veins, and that has undergone extensive mylonitization. The common features of all the Meatiq samples are the lack of active serpentinization and the presence of carbonate alteration that increases from Lz-serpentinite to Atg-serpentinite and talc-rich rocks. The sampling site is completely dry, and thus no fluid samples were collected (for field site images, see Boskabadi et al., 2017).

δ^{60}Ni and δ^{13}C Composition of Fluid and Solid Samples at Tekirova

The dissolved Ni in fluids shows strong variations in both total Ni concentration and δ^{60}Ni values: from 0.21 to 0.96 ppm and +0.41 ± 0.09 to +1.77 ± 0.26‰, respectively. Solid δ^{60}Ni values are dominantly positive, ranging from −0.05 ± 0.07‰ to +0.38 ± 0.06‰ (**Figure 6**; **Table 2**) with an average value of +0.19 ± 0.26‰ ($n = 6$), all of which lie within previously reported ranges for mafic and ultramafic rocks (Ratié et al., 2015). The serpentine-rich, dark-colored BFE samples have δ^{60}Ni values (+0.25 ± 0.03‰) similar to those of the light-colored calcites, brucite-rich veins, and fracture fillings, with δ^{60}Ni values of +0.18 ± 0.06‰. Corresponding δ^{13}C values are −20.53 ± 0.15‰ for serpentines and heavier values of −15.56 ± 0.15‰ for the brucites and veins. Calcite-dominated samples show δ^{13}C values of approximately −23‰. The IR sample shows the lightest values of both δ^{60}Ni and δ^{13}C, −0.05 ± 0.07‰ and −30.19 ± 0.15‰, respectively. The Lz- and Atg-serpentinites and the talc-rich rocks from the Meatiq area show homogeneous δ^{60}Ni values ranging from +0.09 ± 0.04‰ to +0.16 ± 0.05‰, in agreement with earlier reported values for serpentinites (Gall et al., 2013; Cameron and Vance, 2014; Ratié et al., 2015).

DISCUSSION

The main difference between Tekirova and Meatiq is the degree of serpentinization and the activity at the two sites. Meatiq, situated in the Egyptian desert, is an inactive system without any circulating fluids or gas seeps characteristic of active serpentinization, such as fluids with high pH and seepages of reduced gases such as CH_4 and/or H_2 (Sánchez-Murillo et al., 2014). Tekirova, by contrast, has both alkaline fluids with elevated pH and gases characteristic of active serpentinization (CH_4, H_2, and CO_2). Both sites are strongly serpentinized. Meatiq is almost completely serpentinized, with no preserved olivines or pyroxenes (Boskabadi et al., 2017), whereas the Tekirova

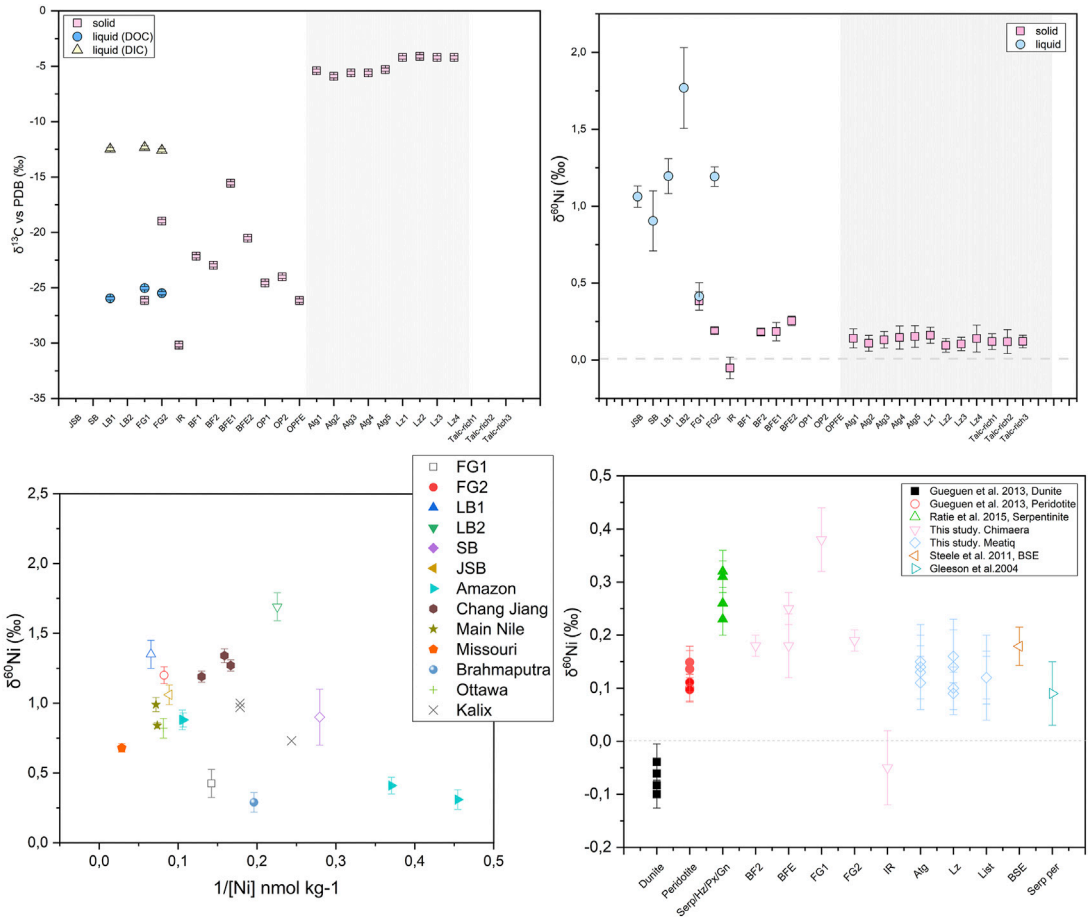

FIGURE 6 | Overview of the Tekirova sampling area. **(A)** δ^{60}Ni shown in square brackets and δ^{13}C in curved brackets. Asterisks mark the solid samples. **(B)** Samples FG1 and FG2 with their characteristic white and red precipitates, respectively. **(C)** Differences in Ca concentration plotted as a function of pH at different serpentinization sites. The Tekirova samples are shown as orange triangles that all fall within the light gray rectangle. The yellow triangles represent the samples from Tekirova analyzed by (Meyer-Dombard et al., 2015; Cameron and Vance, 2014; Gueguen et al., 2013; Ratié et al., 2015; Steele et al., 2011; Gleeson et al., 2004). The two water types are shown in the ovals, where A represents low-pH waters and B high-pH waters.

ophiolite shows a degree of serpentinization between 30 and 65% (Etiope et al., 2011). Both ophiolites show extensive carbonate precipitation, with the distinction that carbonate precipitation at Tekirova is an ongoing event, while only aged carbonates are found at Meatiq.

Fluids at Tekirova

As previously described in Meyer-Dombard et al. (2015), the Tekirova waters are of meteoric origin, affected by active serpentinization at the site. The fluids can be divided into two representative serpentinization water types: 1) high pH and high Ca, and 2) neutral pH and high Ca (**Figure 3**). Compared with similar serpentine seeps, our data represents either a water type more similar to some waters in Cyprus (Neal and Shand, 2002) and Taro-Ceno (Boschetti and Toscani, 2008) with high Ca and neutral to slightly above neutral pH, or a fluid type more similar to Ca-OH^- type waters found in Tekirova (Meyer-Dombard et al., 2015), Voltri (Cipolli et al., 2004), New Caledonia, Oman, and Yugoslavia (Barnes et al., 1978). In contrast to the extremely high concentration of Ca in fluid data presented by Meyer-Dombard et al. (2015), our Ca concentrations are similar to those reported from other serpentine systems (**Figure 6**; Barnes et al., 1978; Cipolli et al., 2004; Boschetti and Toscani, 2008). The contrasting concentrations of Ca may be due to natural fluctuations in the serpentinization rate as well as the overall fluid flow in the area. Both studies were conducted in February during the rainy season, but in contrast to the single fluid seep sampled by Meyer-Dombard et al., we discovered three seeps at the site (**Figure 6**). Thus, a higher fluid flow may explain our diluted values in sampled waters compared to the study by Meyer-Dombard et al. (2015). The intermittent nature of the spring waters of Tekirova, resulting in local and temporal compositional differences, may also explain differences in elemental composition. The larger rivers, SB and JSB, have considerably lower Ni concentrations than the meandering streams on the ophiolite outcrop, with average concentrations of 5.3 and 6.1 nM, respectively, but showed Ni concentrations similar to previously reported values in the Kalix River in Arctic Sweden (2–6 nM) and parts of the Amazon River (4–5 nM; Cameron and Vance, 2014). The meandering streams on the ophiolite, however, show values similar to previously reported values from the Ottawa

TABLE 2 | Overview of the sample mineralogy, $\delta^{13}C$, and $\delta^{60}Ni$ of the samples.

Sample ID	$\delta^{13}C$ vs. PDB (‰)	Specific carbon	Mineralogy	% C	$\delta^{60}Ni/^{58}Ni$ NORM	2SD	Ni (ppm)
Chimaera samples							
Fluid samples							
FG1	−25.03	DOC	—		0.41	0.09	0.66
FG2	−25.49	DOC	—		1.19	0.06	0.69
LB	−25.95	DOC	—		1.19	0.11	0.71
FG1	−12.32	DIC	—		0.44	0.17	0.3
FG2	−12.59	DIC	—		1.21	0.06	0.74
LB	−12.49	DIC	—		1.51	0.06	1.21
LB2			—		1.61	0.09	0.77
LB2			—		1.77	0.26	0.58
SB			—		0.9	0.2	0.26
JSB			—		1.06	0.07	0.21
Solid samples							
BF	−22.15	TotCorg	Carbonates	0.44			
BF	−22.98	TotCorg	Carbonates	0.76	0.18	0.02	2.93
BFE	−15.56	TotCorg	Brucite	0.22	0.18	0.06	1.2
BFE	−20.53	TotCorg	Chrysotile/Mg ferrite	0.06	0.25	0.03	66.78
FG1	−25.94	TotCorg	Carbonates	0.36	0.38	0.06	8.34
FG1	−26.86	TotCorg	Carbonates	0.17			
FG1	−25.61	TotCorg	Serpentine	0.10			
FG2	−18.98	TotCorg	Carbonates/Iron oxides	6.49	0.19	0.02	3.92
IR	−30.19	TotCorg	Iron oxides	1.63	−0.05	0.07	48.9
Meatiq samples							
ATG serpentinite	−5.4				0.14	0.06	22.86
ATG serpentinite	−5.9				0.11	0.05	21.73
ATG serpentinite	−5.6				0.13	0.05	23.1
ATG serpentinite	−5.6				0.15	0.07	23.44
ATG serpentinite	−5.3				0.15	0.07	24.28
LZ serpentinite	−4.2				0.16	0.05	25.16
LZ serpentinite	−4.1				0.09	0.04	22.55
LZ serpentinite	−4.2				0.1	0.04	19.51
LZ serpentinite	−4.2				0.14	0.09	21.47
Talc-rich					0.12	0.05	16
Talc-rich					0.12	0.08	20.2
Talc-rich					0.12	0.04	3.71

River (6–14 nM; Cameron and Vance, 2014, and references therein). The fluid pathways at Tekirova are dominated by percolation of rainwater through the permeable limestone down to the groundwater (Neal and Shand, 2002). Progressive supersaturation of rainwater percolating through the limestone and the contact with high-pH serpentinization fluids initiates carbonate precipitation (visible as red or white precipitates (**Figure 6**) and a concomitant drop in pH. This drop in pH was measured at FG1 and FG2, to pH values of 10.7 and 8.7, respectively. A downhill decrease in the Ca/K ratio from 110 to 57.3 (**Table 3**) is also found to accompany extensive, clearly visible carbonate precipitation.

Carbon Isotopes

Carbon isotopic data of the fluids and solids are very similar to the reported values by Meyer-Dombard et al. (2015). The organic carbon influence decreases down-channel, which is evident also in our data where the total $\delta^{13}C$ is −26.14‰ at FG1 compared with −18.98‰ at FG2 downhill. At FG2, the DIC $\delta^{13}C$ values ($\delta DI^{13}C$) are all close to atmospheric values (**Table 2**) and are thus interpreted as dominantly chemically precipitated calcite, whereas the measured DOC $\delta^{13}C$ ($\delta DO^{13}C$) isotope ratios are indicative of a mixed influence of abiotic seep gases (with a measured $\delta^{13}C$ range between −18 and −26‰; Etiope et al., 2011; Etiope and Sherwood Lollar, 2013) and thermogenic organic matter, as previously reported by Etiope et al. (2011) and Etiope and Sherwood Lollar (2013). At the IR site, however, the $\delta^{13}C$ is as low as −30.2‰, which is likely due in part to the extensive microbial colonization shown in **Figure 4**. The emanating gases were previously discussed by Etiope and Sherwood Lollar (2013), who concluded that the majority of the gas (80–90%) is of abiotic origin, that the remaining 10–20% is thermogenic or microbial, and that the measured $\delta^{13}C$ of carbonates (approximately −11‰; Etiope and Sherwood Lollar, 2013) closely reflects the gas composition. Our $\delta^{13}C$ of −30.2‰ at IR, which is slightly more negative than the previously reported values of −26‰ from the area, may therefore reflect a

TABLE 3 | Table of Tekirova fluid major and minor element compositions, pH, sample coordinates, and major mineralogy.

	LB1	LB2	FG1	FG2	BF1	BF2	IR	JSB	SB	BFE
Coordinates										
	36S0271951/ 4034821	36S0271951/ 4034821	36S0271953/ 4034803	36S0271953/ 4034803	36S0271975/ 4034831	36S0271975/ 4034831				
pH										
	7.6	8.0	10.7	8.7	11.4	11.4	7.9	8.0	9.5	
Major elements (ppm)										
Ca	63.2	52.2	73.7	41.1	23.7	17.8	29.7	22.3	22.3	
K	0.6	0.5	0.7	0.7	0.7	0.7	0.6	0.8	0.8	
Mg	81.9	86.9	32.4	91.8	9.5	8.8	92.5	77.1	77.1	
Na	11.7	11.7	12.3	12.5	7.2	7.3	7.9	8.4	8.4	
S	17.9	17.3	18.0	13.8	8.3	8.0	8.1	8.3	8.3	
Si	37.2	34.8	5.7	29.0	4.9	5.0	31.9	23.2	23.2	
Ca:Mg	0.8	0.6	2.3	0.4	2.5	2.0	0.3	0.3	0.3	
Ni:Fe	0.1	0.7	0.1	0.1	0.2	0.1	0.1	0.1	0.1	
Ca:Fe	1.4	48.8	13.2	0.5	8.6	1.1	5.3	5.7	5.8	
Minor elements (ppm)										
Al	11.2	1.6	3.7	6.2	1.4	2.9	2.3	2.8	2.6	
As	2.3	1.7	2.4	1.2	2.0	1.5	1.9	1.7	1.5	
B	11.0	<DL	2.6	21.6	<DL	4.8	0.5	2.0	1.8	
Ba	7.0	0.6	0.7	0.6	0.7	0.6	0.6	0.6	0.5	
Be	0.0	0.0	0.0	0.0	0.0	<DL	0.0	0.0	<DL	
Co	0.2	<DL	<DL	0.2	0.1	0.1	<DL	<DL	<DL	
Cr	0.9	0.2	0.2	1.4	0.6	0.6	0.4	0.3	<DL	
Cu	0.6	0.5	1.1	1.0	0.6	0.4	0.7	1.1	1.1	
Fe	44.6	1.1	5.6	83.5	2.8	15.8	5.6	3.9	3.8	
Li	0.1	0.1	0.1	0.1	<DL	<DL	0.1	0.1	<DL	
Mn	1.8	0.2	0.2	1.6	0.1	0.8	0.3	0.2	0.3	
Mo	<DL	<DL	<DL	0.1	0.1	<DL	<DL	<DL	<DL	
Ni	4.5	0.8	0.3	4.5	0.5	1.1	0.5	0.4	0.3	
P	2.8	1.9	1.7	16.1	2.4	12.3	6.4	2.5	2.2	
Sr	8.4	7.2	12.4	7.0	8.2	7.0	4.8	3.9	3.9	
Ti	0.3	0.1	0.5	0.3	0.2	0.2	0.2	0.2	0.2	
V	0.2	0.1	<DL	0.1	<DL	<DL	<DL	<DL	<DL	
Zn	2.2	1.3	1.6	3.3	1.0	2.4	1.7	2.0	1.9	
Mineralogy										
Iron oxides				*			*			
	*	*	*	*	*	*	*			*
Serpentine										
Calcite	*	*	*	*	*	*	*			
Aragonite	*	*	*	*			*			
Brucite										*

larger influence of the microbial colonization visible in the sample (**Figure 7**). The large amounts of iron oxides in the IR sample are likely not accumulating ^{12}C (see Zhang et al., 2021) and are thus not likely to be the major cause of the slightly more negative signal seen in the samples. Zhang et al. instead observed an enrichment of ^{13}C in iron oxides, which would, if this process were also prominent at IR, indicate an even stronger fractionation by the microorganisms in the IR sample.

Ni Isotopes

Meteoric fluids generally show a negative correlation between $\delta^{60}Ni$ and [Ni] (Cameron and Vance, 2014), and this is also true for the Tekirova LB samples (**Figure 7**; **Table 2**). The opposite trend can be seen in the FG samples, where increased [Ni] in the fluids is correlated with an increased $\delta^{60}Ni$ value. The [Ni] of the LB samples decreases downhill, and the $\delta^{60}Ni$ increases from +1.35 to +1.69‰, indicating the fractionation of light Ni into the solid precipitates. Fractionation of light Ni into the solid precipitates is also evident in the solid FG samples, where the $\delta^{60}Ni$ changes from +0.38 to +0.19‰. So, even if the dissolved [Ni] and [Fe] increase downhill at the FG site, the precipitation of light Ni is nevertheless indicated at both the LB and FG sites, and the $\Delta^{60}Ni_{solid-fluid}$ at FG increases from 0.03 to 1.02 downhill. The slight change in pH from 7.6 to 8 likely does not influence the carbonate precipitation dramatically (Ruiz-Agudo et al., 2011). Light Ni accumulates in solid precipitates downhill, leaving the

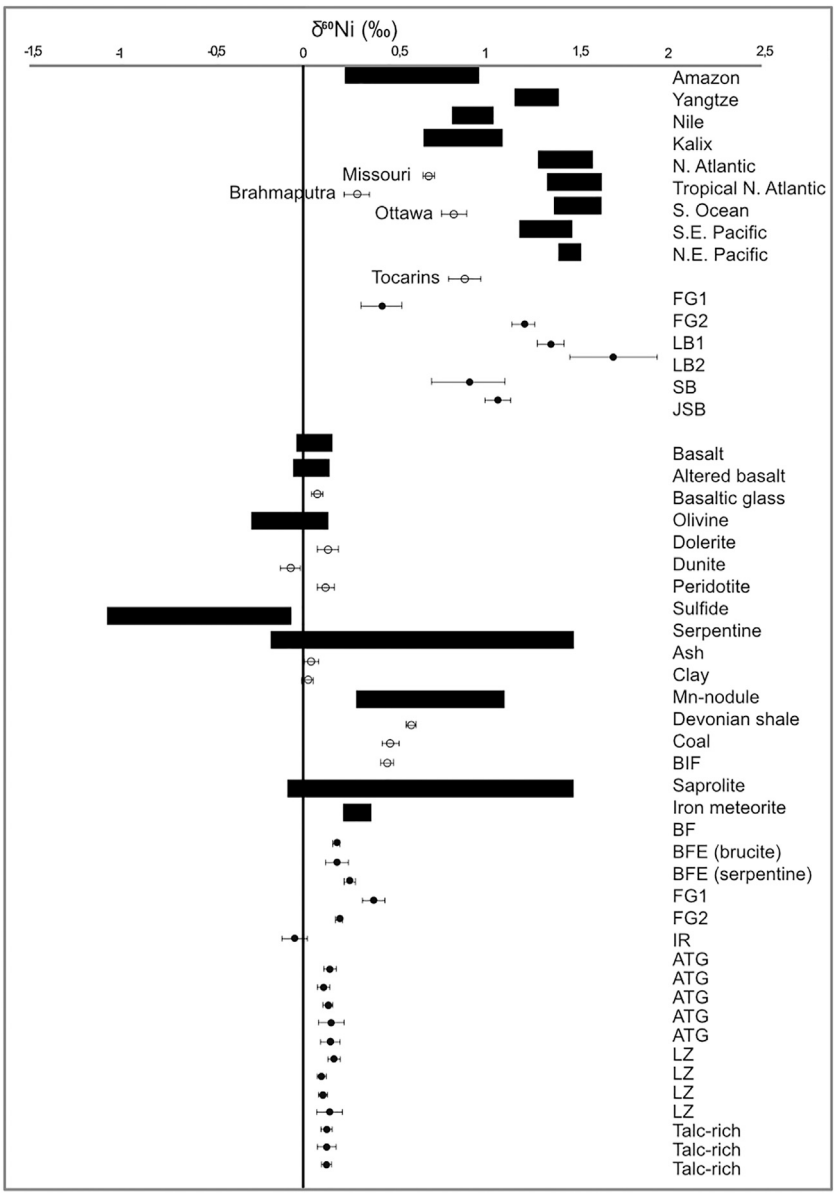

FIGURE 7 | Plot showing $\delta^{13}C$ (upper left panel) and $\delta^{60}Ni$ (upper right panel) in Tekirova and Meatiq (ATG, LZ, and talc-rich samples, shaded area). Pink squares represent solid samples, blue spheres fluid samples, and yellow triangles fluid DIC. Error bars for $\delta^{13}C$ are 0.15‰. The lower left panel shows fluid $\delta^{60}Ni$ values as a function of reciprocal Ni concentration at Tekirova compared with other measured values from Cameron and Vance (2014), marked with an asterisk. Error bars are for long-term reproducibility of standards analyzed using the double spike method. The horizontal gray band gives the average and 1SD of Ni isotope compositions of samples of continental silicate rocks (Cameron et al., 2009). The lower right panel shows $\delta^{60}Ni$ values in this study compared with other studies of rock samples.

stream waters depleted in total [Ni] and light Ni (**Table 2**), similar to what has been reported by Cameron and Vance (2014) and Cameron et al. (2009) for secondary mineralization.

The two FG sites differ in mineral composition; FG2 is composed of iron oxides and carbonates, whereas FG1 is composed purely of carbonates (**Table 2**). It has been shown that light Ni isotopes are preferentially incorporated into iron oxides and calcites during coprecipitation experiments (Eusterhues et al., 2011; Wasylenki et al., 2015; Alvarez, 2019; Neubeck et al., 2021). The preferential uptake of the lighter isotope is coupled to a large surface area and/or growth rate (Alvarez, 2019; Hiemstra et al., 2019). Calcite growth rate is controlled by surface complexation that in turn is controlled by supersaturation and pH (Ruiz-Agudo et al., 2011). At pH values below 8.5, calcite grows mainly by the incorporation of $CaCO_3^0$ at the surface, whereas at pH values greater than 9, Ca^{2+} is also a contributor to the crystal growth due to a faster water exchange rate in the $CaCO_3^0$ ligand. A faster water exchange rate leads to slower calcite precipitation growth, allowing for Ni, which has a slow water exchange rate, to be incorporated into the

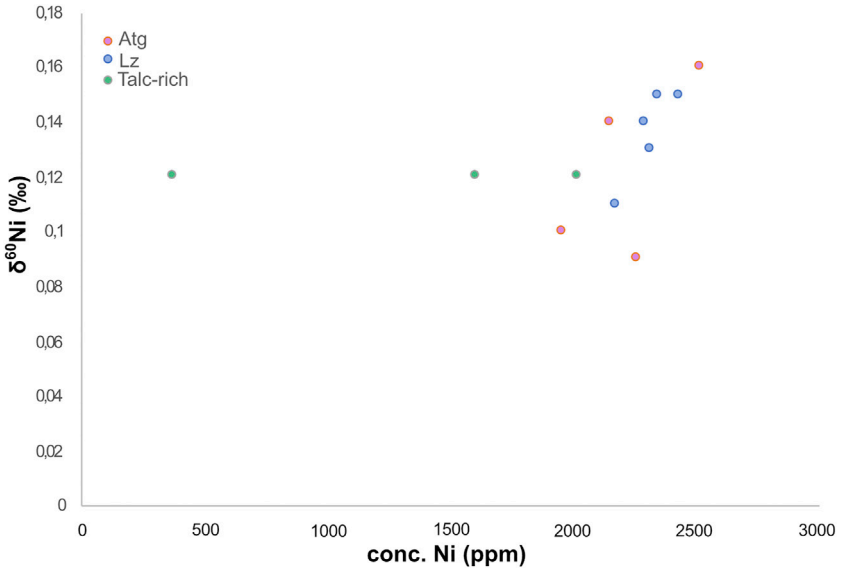

FIGURE 8 | Box plot showing the distribution of δ^{60}Ni values in rivers and oceans and the rock record. The black boxes show the range of δ^{60}Ni values, the open circles show single point values, and the filled circles show the results from this study. Literature values are from Gueguen et al. (2013), Cameron and Vance (2014), and Ratié et al. (2015).

precipitating calcite. Since light Ni is preferentially incorporated into the solid phase, fractionation of Ni isotopes will thus increase with a decreased calcite precipitation rate at higher pH. This effect is likely not very strong at the LB site, where the pH increase is minor. More interesting, then, is the opposite trend observed at the FG sites, where a strong Ni isotope fractionation from +0.43 to +1.2‰ coincides with a dramatic pH drop from 10.7 to 8.7. If calcite precipitation were the only controlling factor for Ni isotopic fractionation, the opposite trend would be observed here. Therefore, we suggest that the precipitation of iron oxides rather than calcite at FG2 controls the precipitation and fractionation of Ni isotopes. This is supported by the downhill mineralogy that shows clear evidence of iron oxides in the solids both in the Raman spectroscopy analyses and in the change of color from white precipitates at FG1 to rusty red at FG2 (**Figure 6**).

The formation of iron oxides is also strongly influenced by pH (Zhu et al., 2016). Any iron-rich fluid that comes in contact with a high-pH fluid such as the FG fluids would immediately induce iron oxide precipitation. This extensive iron oxide precipitation is evident at FG2 both in the Raman spectra (**Figure 4**) that coincide with Raman spectra of natural hematite (De Faria and Lopez, 2007) and in the strong color of the precipitates (**Figure 7**). The δ^{60}Ni signature of +1.2‰ in the fluids at FG2 is consistent with the documented strong fractionation effect that iron oxide precipitates have on Ni isotopes (Wasylenki et al., 2015; Neubeck et al., 2021). At site FG2, the $\Delta^{60}Ni_{solid-fluid}$ is as large as −1.01‰, comparable to reported values of −0.77‰ for adsorption of Ni to goethite under experimental conditions (Gueguen et al., 2013). In Alvarez (2019), carbonate coprecipitation experiments reported $\Delta^{60}Ni_{solid-fluid}$ values close to −1‰, which indicates a stronger effect than our reported value at FG1, where a majority of the precipitates are carbonates, but the $\Delta^{60}Ni_{solid-fluid}$ values are only −0.03‰. This indicates that calcite precipitation has a minor effect on δ^{60}Ni at FG1.

All solid samples (except the IR site with a dominant iron oxide composition and a δ^{60}Ni of −0.05 ± 0.07‰, see below) had δ^{60}Ni values ranging from +0.18 ± 0.02‰ to +0.38 ± 0.06‰, significantly higher than previously reported δ^{60}Ni data from olivines/peridotites (−0.26–0.12‰; Gueguen et al., 2013; Cameron and Vance, 2014; **Figure 8**) or serpentines (−0.13 ± 0.04‰; Gueguen et al., 2013) but similar to reported values for saprolite, which is rich in clays and goethite (Ratié et al., 2015). Meyer-Dombard et al. (2015) showed the presence of clay minerals (montmorillonite) in some samples analyzed from the Tekirova ophiolite, which, if also present in our samples, could likely have had an effect on the δ^{60}Ni values. No XRD analyses were performed in this study, so the influence of clays on the δ^{60}Ni values at Tekirova has yet to be analyzed. The δ^{60}Ni values of the two rivers, SB (+0.90 ± 0.2‰) and JSB (+1.06 ± 0.07‰), are similar to values measured in other rivers globally, with values ranging from +0.31‰ (Rio Negro; Cameron and Vance, 2014) to +1.34‰ (Yangtze; Cameron and Vance, 2014). Even though these values fall within the global range, they are still quite high, likely due to the meandering through areas of active serpentinization, extensive precipitation of light Ni into iron oxides, and possibly other secondary mineralization, leaving the rivers enriched in δ^{60}Ni.

Our enriched δ^{60}Ni data are thus likely due to the ongoing serpentinization with extensive precipitation. The aggregated results from our study indicate that most of our solid samples show positive δ^{60}Ni values. Interestingly, the δ^{60}Ni values of the solid BF samples were similar to the reported values for soil samples (Ratié et al., 2015) or mafic/ultramafic rocks (Gueguen

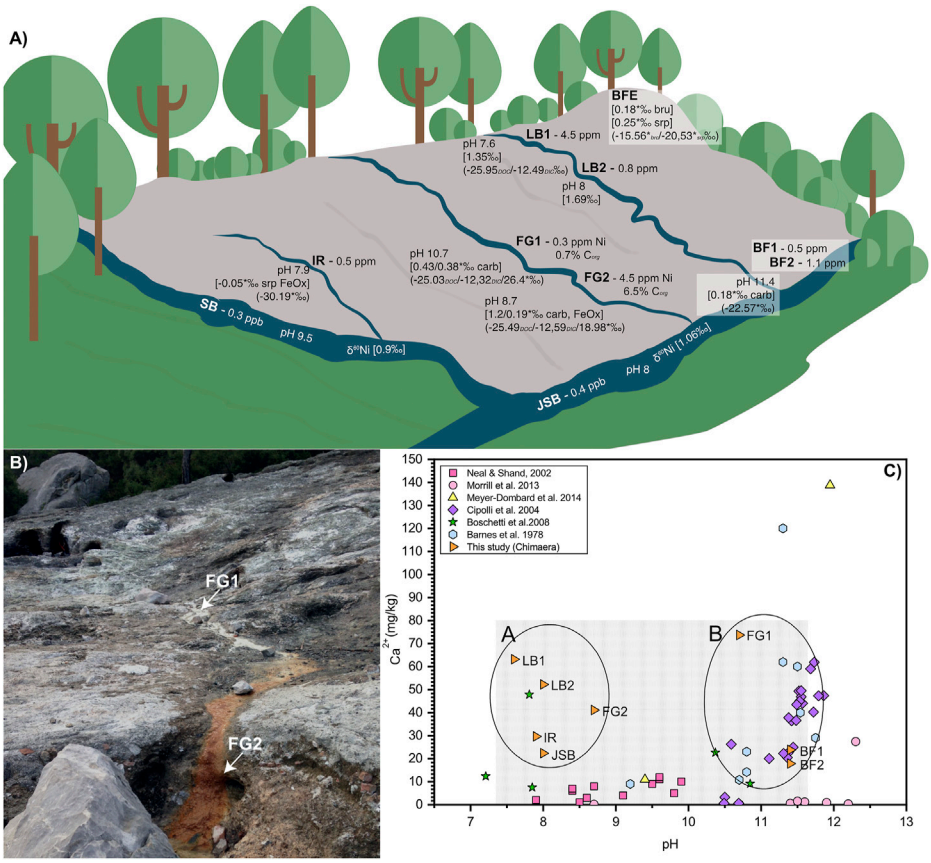

FIGURE 9 | Meatiq sample δ^{60}Ni plotted as a function of Ni concentration (Barnes et al., 1978; Neal and Shand, 2002; Cipolli et al., 2004; Boschetti and Toscani, 2008, Morrill et al., 2013; Meyer-Dombard et al., 2015).

et al., 2013; Cameron and Vance, 2014) despite the large amount of incorporated organic material (**Figure 3**). The same is true for the IR site solid δ^{60}Ni values (−0.05‰) that are similar to reported crustal values (Ratié et al., 2015) but depleted compared with the other local Tekirova samples. This signature coincides with the most negative value of δ^{13}C (**Table 2**). A possible explanation could be the influence of microorganisms and/or iron oxides at the site (Neubeck et al., 2017). Microorganisms, especially methanogens, have been experimentally shown to strongly fractionate stable Ni isotopes (Cameron et al., 2009). Since many methanogens are hydrogenotrophs, using H_2 and CO_2 as energy and carbon sources, the documented seeps of both CO_2 and H_2 (Etiope et al., 2011) at the Tekirova active serpentinization system are likely contributors to fractionation of Ni isotopes. In a recent paper by Zwicker et al. (2018), lipid biomarker evidence for methanogens and methanotrophs was detected within the rocks in the Tekirova ophiolite, strengthening the inference of microbial influence on the IR sample. The SEM images (**Figure 2**) show a clear difference between IR and the other samples, in that the IR sample is completely covered with microorganisms and iron oxides (**Figure 3**). Iron oxides have been experimentally shown to adsorb the lighter Ni isotope and may therefore have an impact on the measured values at the IR site. Other influencing factors on the depleted Ni value are coprecipitation, biologic uptake, or ligand binding (Wasylenki et al., 2007; Fujii et al., 2011; Wasylenki et al., 2015). IR is the only site where light C and Ni coincide, indicating that light Ni may not be easily preserved unless under extensive influence from microorganisms.

Meatiq Ni Isotopes

The solid δ^{60}Ni values of the Meatiq serpentinite all fall within previously reported values for peridotite (Gueguen et al., 2013) and Bulk Silicate Earth (Steele et al., 2011; **Figure 8**). No statistical difference can be seen in δ^{60}Ni average values between the Atg-serpentinite, Lz-serpentinite and talc-rich samples, with average values of 0.14 ± 0.05, 0.12 ± 0.1, and 0.12 ± 0.09‰, respectively. However, plotting δ^{60}Ni as a function of [Ni] shows a positive correlation between δ^{60}Ni and [Ni] in the Atg and Lz samples, whereas no correlation can be observed in the talc-rich samples (**Figure 9**). The talc-rich samples represent greenschist facies high in carbonate (dolomites and magnesites) and low in sulfides, similar to the Atg samples that are subjected to high-temperature alteration (350–400°C), which are rich in carbonates and low in sulfides. The Lz sample, on the other hand, contains few carbonates and high amounts of sulfides (pentlandite and millerite), and represents lower alteration temperatures

(150–250°C) compared to Atg and talc-rich samples. The correlation between δ^{60}Ni and [Ni] looks quite different, as the talc-rich samples do not seem to show any variation with changing [Ni]. This pattern is likely due to homogenization of the samples, which have undergone high-temperature alteration (>400°C) and mylonitization (Boskabadi et al., 2017). These results therefore indicate that the presence of sulfides in serpentines does not have a profound effect on the δ^{60}Ni, at least as long as the concentration of S is quite low (below 800 ppm). The Meatiq samples all have S contents below 800 ppm, and only the Lz samples have visible mineral sulfide grains (see Figure 15E in Boskabadi et al., 2017). Nor does the abundance of carbonates seem to have an effect on the small differences in Ni isotope values between the Meatiq samples, where the Lz contain the smallest amount of carbonates and the talc-rich rocks contain the most carbonates. A possible explanation for the lack of isotopic differences between the serpentine rocks at Meatiq could be the aging effect of carbonates, reducing any isotopic fractionation over time. Another explanation would be that the main source of Ni, which is serpentine, is overprinting any Ni isotopic signature of the carbonates, leading to the similar isotopic compositions observed in the Meatiq samples.

CONCLUSION

Stable Ni isotopic values of solid, carbonate-rich serpentinite rocks and precipitates from two different ophiolites showed absolute values similar to previously reported data on serpentines, ranging from approximately 0.1–0.4‰. The $\Delta^{60}Ni_{solid-fluid}$ values of −1‰ likely reflect the preferential uptake of light Ni into carbonates and/or iron oxides, as previously demonstrated in laboratory experiments. However, the influence of iron oxides on Ni isotope fractionation seems to be stronger than the influence of carbonates. Stable Ni isotopes of the meteoric fluids and solid rock samples from the Tekirova ophiolite indicate that light Ni is preferentially removed from fluids and concentrated into solid phases due to secondary mineral scavenging of light Ni. In one sample, a locally depleted δ^{60}Ni signal coincided with depleted δ^{13}C, likely due to microbial colonization or adsorption onto iron oxides or a combination of these. In summary, it is likely that an active serpentinization system will show enriched δ^{60}Ni values in the fluids but absolute values of the solids similar to those of inactive systems. However, the active system shows more variable values than the inactive system, where the solid δ^{60}Ni values are relatively homogeneous, likely due to aging of the secondary minerals.

DATA AVAILABILITY STATEMENT

The original contributions presented in the study are included in the article/**Supplementary Material**, further inquiries can be directed to the corresponding author.

AUTHOR CONTRIBUTIONS

AN conceptualized the work, performed the data analyses and interpretation and drafted the article. AN, HH, DÖ, and MI performed the field sampling in Turkey, and AB performed the field sampling in Egypt. AB performed the Ni isotope lab analyses. All authors critically reviewed the final draft and approved the final version.

FUNDING

The authors would like to thank the Swedish Research Council (contract no. 2017-05018 to AN, and 2017-04129 to MI) and the Swedish Collegium for Advanced Study for sponsoring this work.

ACKNOWLEDGMENTS

The authors would like to thank Christophe Dupraz for help with fluorescence microscopy. The authors would also like to thank the two reviewers that, with their valuable input, greatly improved the manuscript.

SUPPLEMENTARY MATERIAL

The Supplementary Material for this article can be found online at: https://www.frontiersin.org/articles/10.3389/feart.2021.651967/full#supplementary-material

REFERENCES

Aldanmaz, E., Schmidt, M. W., Gourgaud, A., and Meisel, T. (2009). Mid-ocean ridge and Supra-subduction Geochemical Signatures in Spinel–Peridotites from the Neotethyan Ophiolites in SW Turkey: Implications for Upper Mantle Melting Processes. *Lithos* 113 (3-4), 691–708. doi:10.1016/j.lithos.2009.03.010

Alvarez, M. C. C. (2019). *Nickel Isotope Fractionation during Adsorption on the Calcite Surface and Coprecipitation with Calcite*. Toulouse, France: Université Toulouse 3 - Paul Sabatier. dissertation.

Andresen, A., El-Rus, M. A. A., Myhre, P. I., Boghdady, G. Y., and Corfu, F. (2009). U-pb TIMS Age Constraints on the Evolution of the Neoproterozoic Meatiq Gneiss Dome, Eastern Desert, Egypt. *Int. J. Earth Sci. (Geol Rundsch)* 98, 481–497. doi:10.1007/s00531-007-0276-x

Barnes, I., O'Neil, J. R., and Trescases, J. J. (1978). Present Day Serpentinization in New Caledonia, Oman and Yugoslavia. *Geochimica et Cosmochimica Acta* 42, 144–145. doi:10.1016/0016-7037(78)90225-9

Boschetti, T., and Toscani, L. (2008). Springs and Streams of the Taro-Ceno Valleys (Northern Apennine, Italy): Reaction Path Modeling of Waters Interacting with Serpentinized Ultramafic Rocks. *Chem. Geology.* 257, 76–91. doi:10.1016/j.chemgeo.2008.08.017

Boskabadi, A., Pitcairn, I. K., Broman, C., Boyce, A., Teagle, D. A. H., Cooper, M. J., et al. (2017). Carbonate Alteration of Ophiolitic Rocks in the Arabian-Nubian Shield of Egypt: Sources and Compositions of the Carbonating Fluid and

Implications for the Formation of Au Deposits. *Int. Geology. Rev.* 59, 391–419. doi:10.1080/00206814.2016.1227281

Cameron, V., Vance, D., Archer, C., and House, C. H. (2009). A Biomarker Based on the Stable Isotopes of Nickel. *Proc. Natl. Acad. Sci.* 106, 10944–10948. doi:10.1073/pnas.0900726106

Cameron, V., and Vance, D. (2014). Heavy Nickel Isotope Compositions in Rivers and the Oceans. *Geochimica et Cosmochimica Acta* 128, 195–211. doi:10.1016/j.gca.2013.12.007

Cipolli, F., Gambardella, B., Marini, L., Ottonello, G., and Vetuschi Zuccolini, M. (2004). Geochemistry of high-pH waters from serpentinites of the Gruppo di Voltri (Genova, Italy) and reaction path modeling of CO2 sequestration in serpentinite aquifers. *Appl. Geochem.* 19, 787–802. doi:10.1016/j.apgeochem.2003.10.007

De Faria, D. L. A., and Lopes, F. N. (2007). Heated Goethite and Natural Hematite: Can Raman Spectroscopy Be Used to Differentiate Them?. *Vibrational Spectrosc.* 45, 117–121. doi:10.1016/j.vibspec.2007.07.003

Demirel, I. H., and Gunay, Y. (2000). Tectonic and Karstic Effects on the Western Taurus Region, Southwestern Turkey: Relations to the Present Temperature Gradients and Total Organic Carbon Content. *Energ. Sourc.* 22, 431–441. doi:10.1080/00908310050013848

Dupraz, C., Fowler, A., Tobias, C., and Visscher, P. T. (2013). Stromatolitic Knobs in Storr's Lake (San Salvador, Bahamas): a Model System for Formation and Alteration of Laminae. *Geobiology* 11 (6), 527–548. doi:10.1111/gbi.12063

Etiope, G., Schoell, M., and Hosgörmez, H. (2011). Abiotic Methane Flux from the Chimaera Seep and Tekirova Ophiolites (Turkey): Understanding Gas Exhalation from Low Temperature Serpentinization and Implications for Mars. *Earth Planet. Sci. Lett.* 310, 96–104. doi:10.1016/j.epsl.2011.08.001

Etiope, G., and Sherwood Lollar, B. (2013). Abiotic Methane on Earth. *Rev. Geophys.* 51 (2), 276–299. doi:10.1002/rog.20011

Eusterhues, K., Rennert, T., Knicker, H., Kögel-Knabner, I., Totsche, K. U., and Schwertmann, U. (2011). Fractionation of Organic Matter Due to Reaction with Ferrihydrite: Coprecipitation versus Adsorption. *Environ. Sci. Technol.* 45 (2), 527–533. doi:10.1021/es1023898

Fujii, T., Moynier, F., Dauphas, N., and Abe, M. (2011). Theoretical and Experimental Investigation of Nickel Isotopic Fractionation in Species Relevant to Modern and Ancient Oceans. *Geochimica et Cosmochimica Acta* 75, 469–482. doi:10.1016/j.gca.2010.11.003

Gall, L., Williams, H. M., Siebert, C., Halliday, A. N., Herrington, R. J., and Hein, J. R. (2013). Nickel Isotopic Compositions of Ferromanganese Crusts and the Constancy of Deep Ocean Inputs and continental Weathering Effects over the Cenozoic. *Earth Planet. Sci. Lett.* 375, 148–155. doi:10.1016/j.epsl.2013.05.019

Gleeson, S. A., Herrington, R. J., Durango, J., Velásquez, C. A., and Koll, G. (2004). The Mineralogy and Geochemistry of the Cerro Matoso S.A. Ni Laterite Deposit, Montelibano, Colombia. *Econ. Geology.* 99 (6), 1197–1213. doi:10.2113/gsecongeo.99.6.1197

Gueguen, B., Rouxel, O., Ponzevera, E., Bekker, A., and Fouquet, Y. (2013). Nickel Isotope Variations in Terrestrial Silicate Rocks and Geological Reference Materials Measured by MC-ICP-MS. *Geostand Geoanal Res.* 37, 297–317. doi:10.1111/j.1751-908x.2013.00209.x

Hiemstra, T., Mendez, J. C., and Li, J. (2019). Evolution of the Reactive Surface Area of Ferrihydrite: Time, pH, and Temperature Dependency of Growth by Ostwald Ripening. *Environ. Sci. Nano* 6 (3), 820–833. doi:10.1039/c8en01198b

Hosgörmez, H., Etiope, G., and Yalçin, M. N. (2008). New Evidence for a Mixed Inorganic and Organic Origin of the Olympic Chimaera Fire (Turkey): a Large Onshore Seepage of Abiogenic Gas. *Geofluids* 8, 263–273. doi:10.1111/j.1468-8123.2008.00226.x

Hosgörmez, H. (2007). Origin of the Natural Gas Seep of Çirali (Chimera), Turkey: Site of the First Olympic Fire. *J. Asian Earth Sci.* 30, 131–141. doi:10.1016/j.jseaes.2006.08.002

Lang, S. Q., Bernasconi, S. M., and Früh-Green, G. L. (2012). Stable Isotope Analysis of Organic Carbon in Small (Mg C) Samples and Dissolved Organic Matter Using a GasBench Preparation Device. *Rapid Commun. Mass. Spectrom.* 26, 9–16. doi:10.1002/rcm.5287

Meyer-Dombard, D. R., Woycheese, K. M., Yargıçoğlu, E. N., Cardace, D., Shock, E. L., Güleçal-Pektas, Y., et al. (2015). High pH Microbial Ecosystems in a Newly Discovered, Ephemeral, Serpentinizing Fluid Seep at Yanartaş (Chimera), Turkey. *Front. Microbiol.* 5, 723. doi:10.3389/fmicb.2014.00723

Morrill, P. L., Kuenen, J. G., Johnson, O. J., Suzuki, S., Rietze, A., Sessions, A. L., et al. (2013). Geochemistry and Geobiology of a Present-Day Serpentinization Site in California: the Cedars. *Geochimica et Cosmochimica Acta* 109, 222–240. doi:10.1016/j.gca.2013.01.043

Moynier, F., Blichert-Toft, J., Telouk, P., Luck, J.-M., and Albarède, F. (2007). Comparative Stable Isotope Geochemistry of Ni, Cu, Zn, and Fe in Chondrites and Iron Meteorites. *Geochimica et Cosmochimica Acta* 71, 4365–4379. doi:10.1016/j.gca.2007.06.049

Neal, C., and Shand, P. (2002). Spring and Surface Water Quality of the Cyprus Ophiolites. *Hydrol. Earth Syst. Sci.* 6, 797–817. doi:10.5194/hess-6-797-2002

Neubeck, A., Hemmingsson, C., Boosman, A., Rouxel, O., and Bohlin, M. (2021). Ni Isotope Fractionation during Coprecipitation of Fe(III)(oxyhydr)oxides in Si Solutions. *Geochemistry* 81 (1), 125714. doi:10.1016/j.chemer.2020.125714

Neubeck, A., Sun, L., Müller, B., Ivarsson, M., Hosgörmez, H., Özcan, D., et al. (2017). Microbial Community Structure of a Serpentine-Hosted Abiotic Gas Seepage at the Tekirova Ophiolite, Turkey. *Appl. Environ. Microbiol.* 83, e03430–16. doi:10.1128/aem.03430-16

Ratié, G., Jouvin, D., Garnier, J., Rouxel, O., Miska, S., Guimarães, E., et al. (2015). Nickel Isotope Fractionation during Tropical Weathering of Ultramafic Rocks. *Chem. Geology.* 402, 68–76. doi:10.1016/j.chemgeo.2015.02.039

Ruiz-Agudo, E., Putnis, C. V., Rodriguez-Navarro, C., and Putnis, A. (2011). Effect of pH on Calcite Growth at Constant Ratio and Supersaturation. *Geochimica et Cosmochimica Acta* 75, 284–296. doi:10.1016/j.gca.2010.09.034

Sánchez-Murillo, R., Gazel, E., Schwarzenbach, E. M., Crespo-Medina, M., Schrenk, M. O., Boll, J., et al. (2014). Geochemical Evidence for Active Tropical Serpentinization in the Santa Elena Ophiolite, Costa Rica: An Analog of a Humid Early Earth?. *Geochem. Geophys. Geosyst.* 15 (5), 1783–1800. doi:10.1002/2013gc005213

Spivak-Birndorf, L. J., Wang, S.-J., Bish, D. L., and Wasylenki, L. E. (2018). Nickel Isotope Fractionation during continental Weathering. *Chem. Geology.* 476, 316–326. doi:10.1016/j.chemgeo.2017.11.028

Steele, R. C. J., Elliott, T., Coath, C. D., and Regelous, M. (2011). Confirmation of Mass-independent Ni Isotopic Variability in Iron Meteorites. *Geochimica et Cosmochimica Acta* 75 (24), 7906–7925. doi:10.1016/j.gca.2011.08.030

Stern, R. J., and Gwinn, C. J. (1990). Origin Of Late Precambrian Intrusive Carbonates, Eastern Desert Of Egypt Andsudan: C, O And Sr Isotopic Evidence. *Precambrian Res.* 46, 259–272.

Wasylenki, L. E., Anbar, A. D., Liermann, L. J., Mathur, R., Gordon, G. W., and Brantley, S. L. (2007). Isotope Fractionation during Microbial Metal Uptake Measured by MC-ICP-MS. *J. Anal. Spectrom.* 22, 905. doi:10.1039/b705476a

Wasylenki, L. E., Howe, H. D., Spivak-Birndorf, L. J., and Bish, D. L. (2015). Ni Isotope Fractionation during Sorption to Ferrihydrite: Implications for Ni in Banded Iron Formations. *Chem. Geology.* 400, 56–64. doi:10.1016/j.chemgeo.2015.02.007

Wasylenki, L., Wells, R., and Frierdich, A. (2019). *Ionic Strength Strongly Affects Ni Isotope Fractionation between Solution and Mn Oxyhydroxide*. Barcelona: Goldschmidt. doi:10.1130/abs/2019am-338990

Woodcock, N. H., and Robertson, A. H. F. (1977). Origins of Some Ophiolite-Related Metamorphic Rocks of the "Tethyan" belt. *Geol* 5 (6), 373–376. doi:10.1130/0091-7613(1977)5<373:oosomr>2.0.co;2

Zhang, Y., Gan, Y., Yu, K., and Han, L. (2021). Fractionation of Carbon Isotopes of Dissolved Organic Matter Adsorbed to Goethite in the Presence of Arsenic to Study the Origin of DOM in Groundwater. *Environ. Geochem. Health* 43 (3), 1225–1238. doi:10.1007/s10653-020-00644-w

Zhu, M., Frandsen, C., Wallace, A. F., Legg, B., Khalid, S., Zhang, H., et al. (2016). Precipitation Pathways for Ferrihydrite Formation in Acidic Solutions. *Geochimica et Cosmochimica Acta* 172, 247–264. doi:10.1016/j.gca.2015.09.015

Zwicker, J., Birgel, D., Bach, W., Richoz, S., Smrzka, D., Grasemann, B., et al. (2018). Evidence for Archaeal Methanogenesis within Veins at the Onshore Serpentinite-Hosted Chimaera Seeps, Turkey. *Chem. Geology.* 483, 567–580. doi:10.1016/j.chemgeo.2018.03.027

Conflict of Interest: The authors declare that the research was conducted in the absence of any commercial or financial relationships that could be construed as a potential conflict of interest.